

Rare-earth-free zinc aluminium borate white phosphors for LED lighting

P. Gaffuri,^{a,b} M. Salaün,^a I. Gautier-Luneau,^a G. Chadeyron,^c A. Potdevin,^c L. Rapenne,^b E. Appert,^b V. Consonni,^b A. Ibanez,^a

FOOTNOTES

^a Univ. Grenoble Alpes, CNRS, Grenoble INP, Institut Néel, 38000 Grenoble, France.

^b Univ. Grenoble Alpes, CNRS, Grenoble INP, LMGP, 38000 Grenoble, France.

^c Université Clermont Auvergne, CNRS, SIGMA Clermont, Institut de Chimie de Clermont-Ferrand, F-63000, Clermont-Ferrand, France.

Corresponding author's e-mail: Mathieu.salaun@neel.cnrs.fr

Electronic Supplementary Information (ESI) available.

ABSTRACT

The use of rare-earth elements (Y, Ce, Eu...) in commercial phosphor-converted white light-emitting diodes (pc-WLEDs) raises environmental and geopolitical concerns. Lanthanide-free white emitting phosphors based on amorphous yttrium aluminium borate (YAB) have previously been synthesized by the polymeric precursor (PP) method, showing high internal quantum yields (iQY) and a broad emission band in the visible range. However, yttrium has still been largely present in the amorphous YAB matrix. Here we synthesize zinc aluminium borate (ZAB) powder by the PP method, a novel family of rare-earth-free phosphor producing broad and intense photoluminescence emissions when excited by near-UV from 300 to 400 nm, with high iQYs up to 60%. The photoluminescence band is easily tuneable in the visible range of the electromagnetic spectrum, from warm- to cold-white emissions by adjusting either the precursor ratio or the calcination temperature used to prepare the ZAB powders. Finally, we report spectroscopic arguments that reinforce the hypothesis of the molecular origin of the photoluminescence in ZAB phosphors. Our results demonstrate the essential role of the composition (Al / B ratio) and thermal treatment in the transformation and trapping of carbonaceous species (*i.e.* black carbon or luminescent molecular species) in amorphous ZAB matrix. This efficient family of phosphors only composed of abundant and non-toxic elements opens the way

for the integration of rare-earth-free single phosphors synthesized by wet chemistry into WLEDs lighting devices.

INTRODUCTION

Phosphor-converted white light emitting diodes (pc-WLEDs) have recently dominated the lighting market through their energy efficiency, stability, and ease of integration into smart lighting technologies, thanks to the development of efficient blue- and near-UV (NUV) emitting gallium nitride based LEDs¹⁻³ that excite a phosphor to complete the emission and produce white light. The canonical phosphor for LED lighting consists of the $Y_{3-x}Ce_xAl_5O_{12}$ (YAG:Ce) micron-sized powders emitting around 550 nm, sometimes associated with Eu^{2+} doped sulphide or nitride to obtain warm-white emissions. The strong efficiency of YAG:Ce is related to the unique optical properties of Ce^{3+} ions - *i.e.* fast optical transition from 5d- and 4f-electronic levels - as well as to the good hosting properties of YAG.^{4,5} Nevertheless, the use of rare-earth (RE) elements in such commercial phosphors, as emitter (cerium, europium) and host matrix (yttrium), raises environmental and geopolitical concerns.^{6,7} Thus, efficient RE-free single phosphors, excitable in the blue / NUV range and exhibiting a broad emission band extended in the whole visible range, are strategic materials to be developed, although it remains a major scientific challenge.^{8,9}

On one hand, a tremendous effort has been devoted to the identification of a suitable WLED phosphor matrix to host RE ions,¹⁰⁻¹³ including RE-free matrix, which decreases the overall RE content in phosphors, yet does not remove them completely. On the other hand, phosphors based on a RE-free photoluminescence (PL) have extensively been studied. Among them, defect-related luminescent materials, synthesized by chemical methods, are good candidates since they typically combine high PL efficiency, good stability, ease of fabrication, as well as a broad PL emission.¹⁴ Pioneering works on these materials were done on silicate-based matrices,^{15,16} which now includes phosphates,^{17,18} metal oxides,¹⁹⁻²⁵ boron carbon oxynitride (BCNO),²⁶⁻²⁸ and carbon-based nanomaterials.²⁹ These phosphors are promising, although they generally produce blue or bluish-white light, their quantum efficiencies are not systematically specified, and their PL mechanisms are not fully understood.

Recently, amorphous yttrium aluminium borate (YAB) have been synthesized by the polymeric precursor (PP) method, showing high internal quantum yields (iQY) and a warm-white emission.^{30,31} Amorphous YAB was also synthesized by the sol-gel method, where the emission of polycyclic aromatic hydrocarbon molecules, trapped in the amorphous matrix during the synthesis process of the micron-sized powders, was for the first time evidenced by coupling thermal analyses (differential thermal analysis, thermogravimetry, mass spectrometry), PL spectroscopy, nuclear magnetic resonance and electron paramagnetic resonance measurements coupled with DFT calculations.³² Nevertheless, yttrium was still used in significant amounts to form the glassy aluminium borate matrix, acting as a cation glass network modifier.

In this article, we present a novel matrix of RE-free phosphor made of zinc aluminium borate (ZAB) synthesized by the PP method. The content of zinc, aluminium, and boron is varied, along with the thermal treatment conditions, in order to elucidate their effects on the morphology, the microstructure and the trapping of black carbon and molecular PL emitters in the ZAB network. The corresponding evolution of the PL properties are thoroughly analysed, also by varying the excitation wavelength, to provide spectroscopic insights into the origin of the luminescence in ZAB phosphors.

EXPERIMENTAL

Synthesis method

The preparation of ZAB powders was based on the PP methods, also labelled as modified *Pechini* methods.³⁰ $\text{Zn}(\text{NO}_3)_2 \cdot 6\text{H}_2\text{O}$ (1 g, 99%, Alpha Aesar), $\text{Al}(\text{NO}_3)_3 \cdot 9\text{H}_2\text{O}$ (3.85 to 9.4 g, 99%, Fisher Scientific) and citric acid monohydrate (32 g, Fisher Scientific) were dissolved in 50 mL of ultrapure water (0.63 $\mu\text{S}/\text{cm}$, Fisher Scientific) heated at 80°C under stirring for 15 min. Simultaneously, in a second solution, H_3BO_3 (1.20 to 2.46 g, 99.8%, Fisher Scientific) and D-sorbitol (20 g, Fisher Scientific) were dissolved in 50 mL of ultrapure water heated at 80°C under stirring for 15 min. This polyalcohol has been chosen instead of conventional ethylene glycol to improve boron complexation, thus avoiding boron losses during thermal annealings.^{33,34} The Al / B molar ratio between aluminium and boron precursors were set to 0.25, 0.5, 0.75 and 1.5, while the molar ratio between all inorganic

precursors (Zn, Al and B) and citric acid was kept at 1:3. The two solutions were then mixed together and heated under reflux at 100 °C for 44 hours. The solution was partially evaporated at 80 °C to promote the esterification reactions, leading to a yellowish and viscous resin, which was further dried at 250 °C during 30 min, under air atmosphere. The resulting dried resin was crushed in a planetary mill to obtain fine brown powders, then pyrolysed under N₂ continuous flux at 700°C during 24 hours, releasing a large amount of organic moieties through mainly CO₂ and H₂O losses related to citrate groups decomposition³⁵ without any drastic combustion reactions. Pyrolysed powders were subsequently sieved with a 20 µm stainless steel mesh. Finally, grains with size under 20 µm powders were calcinated at different temperatures ranging from 600 to 1000 °C for 24 hours under O₂, forming the ZAB particles.

Microstructural characterizations

The morphology of ZAB particles was observed in a field emission scanning electron microscope (FESEM) ZEISS Ultra+ operating with an acceleration voltage $V = 20$ kV. Analysis of the chemical composition was carried out on the FESEM equipped with a Bruker EDS system with a Silicon Drift Detector. Transmission electron microscopy (TEM) and scanning transmission electron microscopy (STEM) specimens were prepared by depositing a drop of ZAB powders dispersed in absolute ethanol, onto carbon grids. The surface of the particles was investigated by TEM with a JEOL-JEM 2010 microscope operating at 200 kV with a 0.19 nm point to point resolution. The chemical homogeneity was assessed with STEM-EDS elemental maps of single particles that were collected with a JEOL SDD Centurio detector having a large solid angle of up to 0.98 steradians incorporated in the JEOL 2100F field-emission-gun scanning electron microscope operating at 200 kV and having a 0.2 nm resolution in the scanning mode.

In situ temperature-dependent powder X-ray diffraction (PXRD) was used to record the structural changes occurring during the calcination step. The powder was dispersed on an alumina crucible placed at the focal point of the X-ray (Cu K α 1) incident beam. Diffracted X-rays were recorded from 20° to 120° in 2 θ , under air, from room temperature to 900 °C with a heating rate of 1 °C /min. Room-

temperature PXRD patterns were collected with a Brucker D8 Endeavour diffractometer using Cu radiation in θ - θ configuration.

Optical characterizations

The optical properties were investigated by recording the PL spectra with a Jobin-Yvon set-up consisting of a Xenon lamp operating at 400 W and two monochromators (Triax 550 and Triax 180) combined with a cryogenically cold charge coupled device (CCD) camera (Jobin-Yvon Symphony LN2 series) for emission spectra ($\lambda_{\text{exc}} = 385$ nm) and with a Hamamatsu 980 photomultiplier for excitation ones. IQY efficiencies and absorbance were recorded using C9920-02G PL-QY measurement system from Hamamatsu. The setup comprised a 150W monochromatized Xe lamp, an integrating sphere (Spectralon Coating, $\varnothing = 3.3$ inch) and a high sensitivity CCD spectrometer for detecting the whole spectral luminescence. Trichromatic coordinates were also determined thanks to this equipment. All luminescence experiments were performed at room temperature.

RESULTS AND DISCUSSION

Powder synthesis

ZAB phosphors were synthesized by the PP method, which is suitable to form multi-metal oxides with a high homogeneity at the molecular level.³⁶ This method has previously been used to synthesize YAB particles having a strong and broad PL band in the visible range when excited from 250 to 400 nm.^{30,31,35} In order to synthesize RE-free phosphors, yttrium should be substituted from the composition, but without major modification of the amorphous structure. Zinc was selected to substitute yttrium, as their field strengths (*i.e.* the charge divided by the square of the radius) of 0.52 and 0.53, respectively, are similar^{37,38}. As a result, both cations belong to the category of glass network modifier, according to Dietzel theory.³⁹ Moreover, Zn^{2+} ($3d^{10}$) ions as well as Y^{3+} ($4d^0$) ions do not give rise to any absorption in the NUV and visible region.

The powders with the strongest PL were obtained with a Al / B precursor molar ratios of 0.25, 0.5, and 0.75 and a constant ZnO molar ratio of 12%. Photographs of those three optimized ZAB powders under daylight illumination and under 365 nm excitation are shown in Fig. 1a and 1b, respectively, as

a function of the calcination temperature (T_{Ca}) ranging from 600 to 750°C. Before the calcination step, the black colour of carbon-rich pyrolysed powder is attributed to the presence of black carbon arising from the decomposition of organic precursors, as confirmed by the typical Raman bands of such disordered carbon shown in Fig. S1.^{40–42} Accordingly, the brown colour under daylight illumination of powders calcined with low T_{Ca} is attributed to the remaining of small clusters of black carbon formed during the pyrolysis step.³⁶ When T_{Ca} is raised, this trapped black carbon is further oxidized and released as CO_2 gas, as shown by thermogravimetric analysis (TGA) coupled with differential thermal analysis (DTA) and mass spectrometry (MS) (Fig. S2), as well as SEM-EDS (Fig. S3), leading to the whitening of the powder. Interestingly, the whitening of the powder occurs at a lower T_{Ca} when the Al / B ratio is increased. Indeed, as shown in Fig. S2, the mass ratio of carbon in calcinated ZAB powder at 600°C is less than 1%, 5%, and 20% for Al / B ratios of 0.75, 0.5 and 0.25, respectively, evidencing the lower carbon trapping of the matrix when the Al / B ratio is increased.

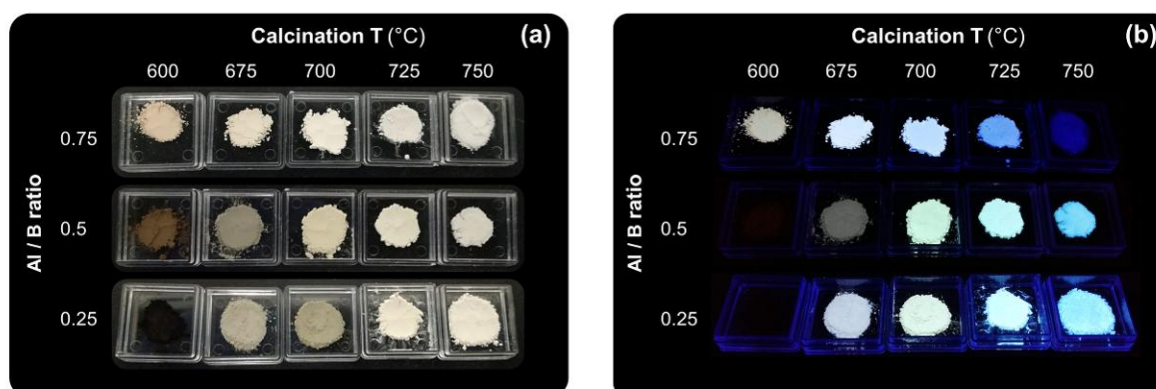


Fig. 1 (a) Photographs of the optimized ZAB phosphor powders, under daylight and (b) under NUV illumination at 365 nm.

Similarly, the luminescence is strongly affected by T_{Ca} . No PL emission occurs with the naked eye in the ZAB particles calcinated at a low temperature (Fig. 1b), due to the large amount of black carbon they contain and which absorbs all lights. Increasing the T_{Ca} leads to a warmer PL under NUV, particularly for Al / B ratios of 0.25 and 0.5, which is blue shifted by further raising the T_{Ca} , regardless of the Al / B ratio of the ZAB particles. Finally, the ZAB powders lose their PL properties for a T_{Ca} comprised between 750 and 800 °C (Fig. S4). Hence, there is an optimum T_{Ca} range, at which the ZAB powders possess strong PL properties and the suitable warm-white emission.

The chemical purity of the three optimized powders was assessed by SEM-EDS, as shown in [Fig. S5a](#) where the absence of peaks related to other chemical elements in the EDS spectra is clearly shown, considering the high electron acceleration voltage of 20 kV. The inset shows an enlargement of the SEM-EDS spectra normalized with respect to the oxygen peak. The good match between the decrease in the Al / B precursor ratios and the decrease in the intensity of the Al K α peak shows the successful adjustment of the composition of the final oxide particles.

Finally, in addition to the optimized compositions, Fig. S5b shows the other chemical compositions tested which are very weakly or not luminescent (as observed in Fig. S4), due to the formation of crystallized solids, as specified in the following paragraph on particle microstructure.

Particle morphology

The morphology of the ZAB particles is shown in the FESEM micrograph in Fig. 2a. A representative particle with a Al / B ratio of 0.75 and T_{Ca} of 675 °C presents a smooth surface and conchoidal fractures (Fig. 2b) characteristic of a glassy structure, as previously observed in YAB phosphors.⁴³ On the other hand, a typical particle with Al / B ratio of 0.25 also calcinated at 675 °C has a rough surface (Fig. 2c). Indeed, the surface of such particles was observed at higher magnification by TEM, showing a thin shell of crystalline nanowires indexed as phase similar to Al₄B₂O₉,⁴⁴ as shown in Fig. 2d, 2e, and S6. These surface differences between Al-rich and B-rich particles are highlighted for a T_{Ca} of 700°C in Fig. S7, while varying the chemical composition had no significant effect on particle size. Finally, raising T_{Ca} to 1000 °C leads to the formation of entangled non-luminescent whiskers for all Al / B ratios (Fig. S8 and S4) due to deep particle crystallization at very high T_{Ca}.

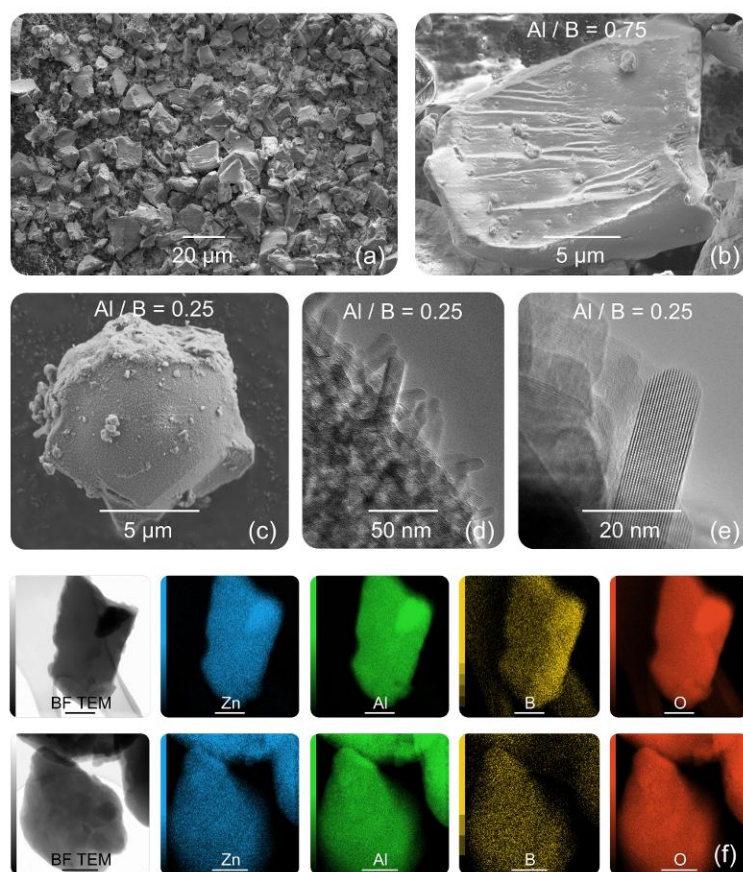


Fig. 2 FESEM micrographs showing (a) a global view of ZAB particles, and single ZAB particles (b) with $Al/B = 0.75$ and (c) with $Al/B = 0.25$. (d-e) Bright-field TEM micrographs of the surface of particles with $Al/B = 0.25$. (f) STEM-EDS elemental maps of ZAB luminescent particles, here for $Al/B = 0.75$, and $T_{Ca} = 650^{\circ}C$, showing their good chemical homogeneity. The scale bars are 250 nm.

EDS elemental maps of glassy ZAB particles calcinated at $T_{Ca} = 650^{\circ}C$ (*i.e.* below their crystallization temperature, see next section) were collected by STEM (see Fig. 2f). No element is shown to be segregated, unlike similar AlBCNO white emitting phosphors.⁴⁵ The more intense regions of the elemental maps are only due to larger probed area in overlapping particles, as shown in the bright-field image. Indeed, the poly-esterification reactions between Al and Zn citrates complexes and the alcoholate boron ones during the first step of the synthesis avoid the segregation of the metal cations during the formation of the oxide network, promoting in turn its high molecular homogeneity.

Particle microstructure

As the exothermic peaks observed in TGA-DTA analyses (Fig. S2) can both be attributed to the crystallization of ZAB powders, and to the calcination of the residual carbonaceous species, the

crystallization behaviour of the powders with Al / B ratios of 0.75 and 0.25 was assessed by *in situ* temperature-dependent XRD (Fig. 3). Besides, contrary to our previous work carried out on YAB vitreous powders,³⁰ we could not clearly identify in this study the glassy transition for ZAB samples on the DTA curves.

Two broad bands of X-ray scattering centred around $2\theta = 25^\circ$ and 45° that are characteristic of the amorphous structure turn into diffraction peaks within a few degrees at around 660°C for both Al / B ratios of 0.25 and 0.5 (Fig. S9). In contrast, for the Al / B ratio of 0.75, the crystallization into the same crystallographic phase is delayed to 775°C , showing the significant effect of the Al / B ratio on the amorphous matrix, between Al / B ratio of 0.5 and 0.75. It has been reported in the literature that increasing the Al content in borate glasses leads to a higher T_g and a decrease in the atomic packing density. This is attributed to an increase of the coordination number of Al from 4 to 5 and 6,^{46,47} observed by solid-state NMR when the Al molar ratio exceed 30%,⁴⁸ i.e. when Al / B > 0.5 in our case. The increase in T_g should account for the increase in crystallization temperature, while the atomic packing density affects the release of carbonaceous moieties from ZAB particles. Indeed, we believe that the larger content of carbon measured in boron-rich particles is due to a denser packing of the amorphous network, thus trapping the carbonaceous species more efficiently during the calcination process. It is remarkable that microstructural considerations in melt-quenched glasses seem to apply to amorphous grains obtained by the PP method.

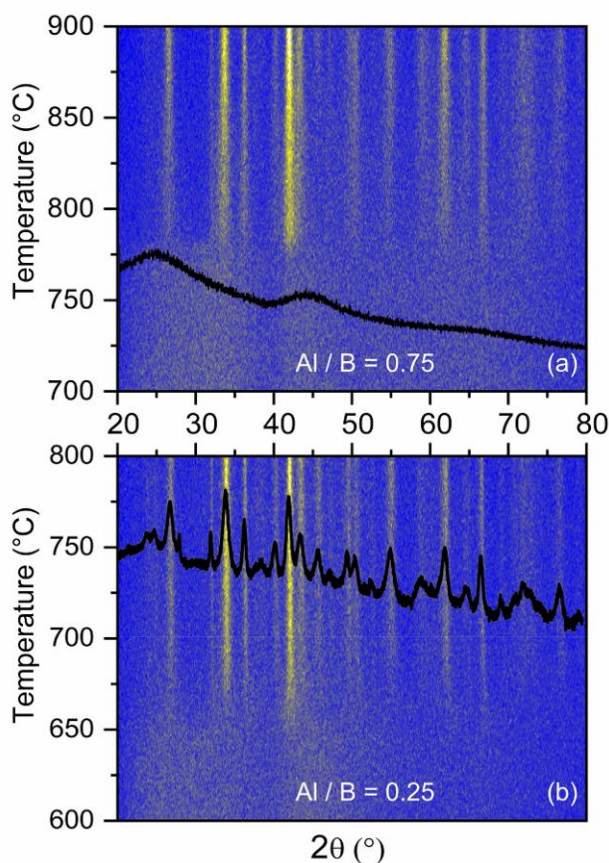


Fig. 3 *In situ temperature-dependent PXRD diffractogram of ZAB particles (previously pyrolysed) calcinated under air for the compositions (a) $Al / B = 0.75$ and (b) $Al / B = 0.25$. To highlight the scattering bands and diffraction peaks, and to overcome the low instrumental counts below $2\theta = 25^\circ$, conventional room-temperature diffractograms of ZAB powder with corresponding Al / B ratio, calcinated at $750^\circ C$, have been superimposed. The diffractogram shown in (b) is indexed in Fig. S10.*

In order to identify the resulting crystalline phases, PXRD patterns were registered. The crystallographic phase could not be found in any databases, yet it showed similarities with that of $Al_4B_2O_9$ together with those of $Cu_2Al_6B_4O_{17}$ or $LiAl_7B_4O_{17}$ (see Powder Diffraction Files 00-029-0010, 04-15-3532 and 00-052-1131 respectively),^{49,50} as shown in Fig. S10, suggesting a zinc aluminium borate phase. Similarly, the first phase to crystalize in YAB phosphors is $Al_4B_2O_9$.³⁰ Very interestingly, the formation of $Cu_2Al_6B_4O_{17}$ whiskers nucleating from the surface of aluminium borate particles, before growing as independent micrometric whiskers at higher temperature, has been reported previously,⁴⁹ similarly to ZAB particles in Fig. S8. Nevertheless, the strong PL of fully amorphous aluminium-rich ZAB phosphors, together with the absence of luminescence in powders

calcinated from 800 to 1000°C (Fig. S4), rich in the crystalline phase, rules out the hypothesis of luminescent crystalline phase.

The FESEM and TEM micrographs, together with the analogy with the $\text{Cu}_2\text{Al}_6\text{B}_4\text{O}_{17}$ phase clearly indicates that only the surface of boron-rich luminescent ZAB particles crystallizes at 660 °C, leaving a large amorphous core where carbonaceous species are trapped. Inversely, the composition leading to non-luminescent powders (Fig. S4) are characterized by a strong crystallization. Indeed, an increase in the ZnO content from 12 % to 20 % led to sharp peaks corresponding to ZnB_4O_7 , in addition to the previous metal aluminium borate phase (Fig. S11), and the removal of Al led to sharp peaks corresponding to ZnB_4O_7 as well as $\text{B}(\text{OH})_3$ (Fig. S12). We correlate this crystallization and phase segregation with their non-luminescence due to the loss of molecular emitters during the complete crystallization of the matrix, as observed in ZAB and previously in $\text{YAB}^{30,35}$ phosphors, when the T_{Ca} is above 800°C (Fig. S4). These observations show that the presence of a large majority of amorphous phase in ZAB phosphors through an optimized metallic precursor ratio is necessary for their luminescence properties.

Photoluminescence properties of ZAB phosphors

In the first part of the article, we showed that Al / B ratios of 0.5 and 0.25 led to similar structural properties in ZAB powders. The rest of the article will focus on Al / B = 0.5, leaving the very similar Al / B = 0.25 in the supporting information, to highlight the critical effect of the composition between Al / B = 0.75 and 0.5 on the PL properties of ZAB phosphors.

Fig. 4 shows the room-temperature emission spectra of ZAB particles under NUV excitation at 385 nm, which corresponds to the typical emission wavelength of some commercial NUV LEDs. This analysis hence allows us to estimate the potential of these phosphors for their application as single white phosphors in NUV LED-based devices.

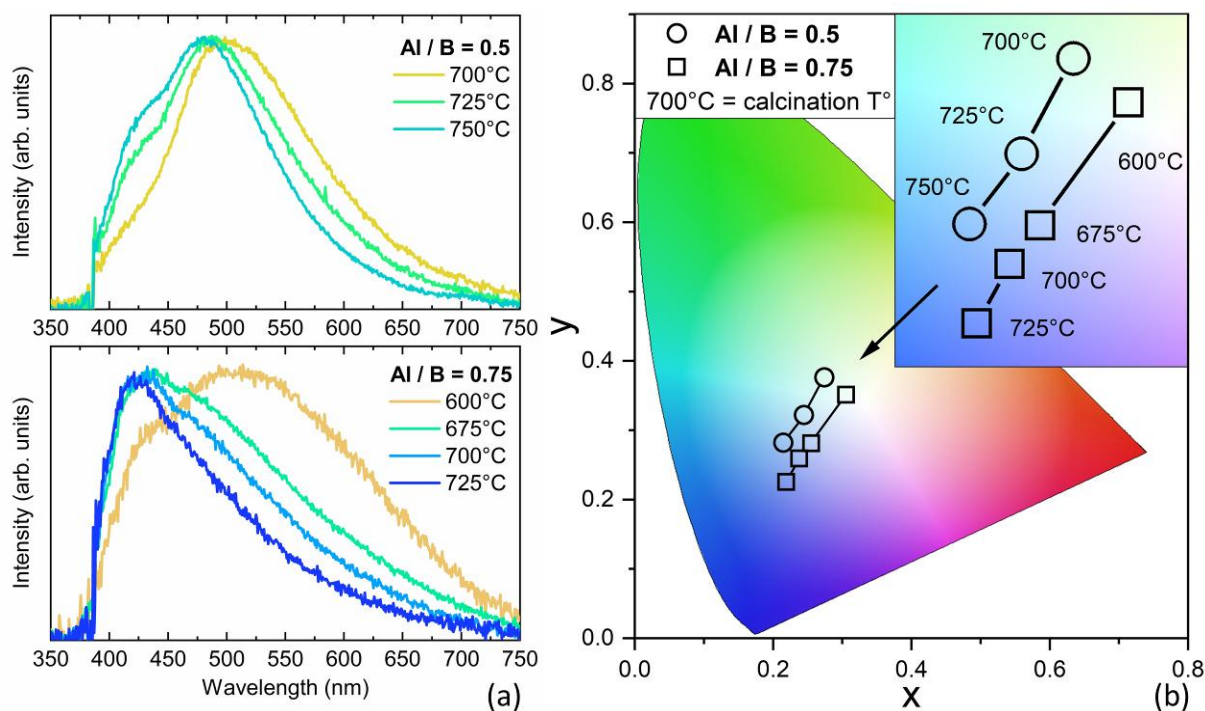


Fig. 4 (a) Normalized room-temperature PL spectra and (b) chromaticity (CIE 1931) of the ZAB particles excited at 385 nm, for $Al/B = 0.5$ and 0.75 , with T_{Ca} ranging from 600 °C to 725 °C and 700 °C to 750 °C, respectively.

The normalized room-temperature PL spectra of ZAB phosphors with Al/B ratios of 0.25, 0.5, and 0.75 are shown in Fig. S13 and Fig. 4a. For all compositions, a broad emission band is observed from 400 to 700 nm which blue shifts by raising T_{Ca} . In the case of the Al/B ratio of 0.5, the PL spectra are centred at 500 nm, and by raising T_{Ca} , the warm colour contribution from 550 to 700 nm decreases in favour of shorter wavelengths from 400 to 450 nm. For the Al/B ratio of 0.75, the PL emission is extended in the whole visible wavelengths for $T_{Ca} = 600$ °C, while it gradually narrows towards shorter wavelengths (400-550 nm) when T_{Ca} is raised from 675 °C to 725 °C. Finally, the PL spectra and the variation with respect to T_{Ca} are very similar for phosphors with the Al/B ratios of 0.25 and 0.5, as seen in Fig. S13.

The corresponding colour points of ZAB phosphors are depicted in Fig. 4b in a standard two-dimensional CIE 1931 chromaticity diagram. As expected, the distribution of emitted photons from ZAB phosphors excited at 385 nm changes from white (pure white being located at $x = y = 0.33$) to bluish emission with increasing T_{Ca} . This blue shift contrasts with the YAB phosphors synthesized by

the PP method as well as by the sol-gel process, where a red shift of the emission band has commonly been observed by raising T_{Ca} ^{30–32}. This can be first attributed to the different role of Zn comparing to Y in the formation and structure of the amorphous network, thus trapping different molecular emitters. Moreover, ZAB particles have a significantly lower diameter and size distribution than YAB phosphors (diameters from 30 to 70 μm) due to the sieving of pyrolysed particle with a 20 μm mesh, which strongly affects particle formation, as well as the oxidation of carbonaceous species during the calcination step. Finally it should be noted here that the PL of ZAB phosphors with the highest Al / B ratio of 0.75 shifts at a significantly lower T_{Ca} than for the other two, similarly to the carbon content (Fig. S2).

The PL iQY, absorbance (Abs) and external quantum yields (eQY) of the most luminescent ZAB phosphors are shown in Fig.5, and correspond to the following formulae:⁵¹

$$iQY = \frac{\text{number of photons emitted}}{\text{number of photons absorbed}} \quad (1)$$

$$Abs = \frac{\text{number of photons absorbed}}{\text{number of incident photons}} \quad (2)$$

$$eQY = iQY \times Abs = \frac{\text{number of photons emitted}}{\text{number of incident photons}} \quad (3)$$

λ_{exc} was set to 385 nm, but also to 305 nm, because the excitation-dependent iQY and Abs measurements showed a maximum for this higher energy value (Fig. S14). iQY and Abs are consistently higher for $\lambda_{exc} = 305$ nm, and follow the same trends when T_{Ca} is varied, regardless of the excitation wavelength.

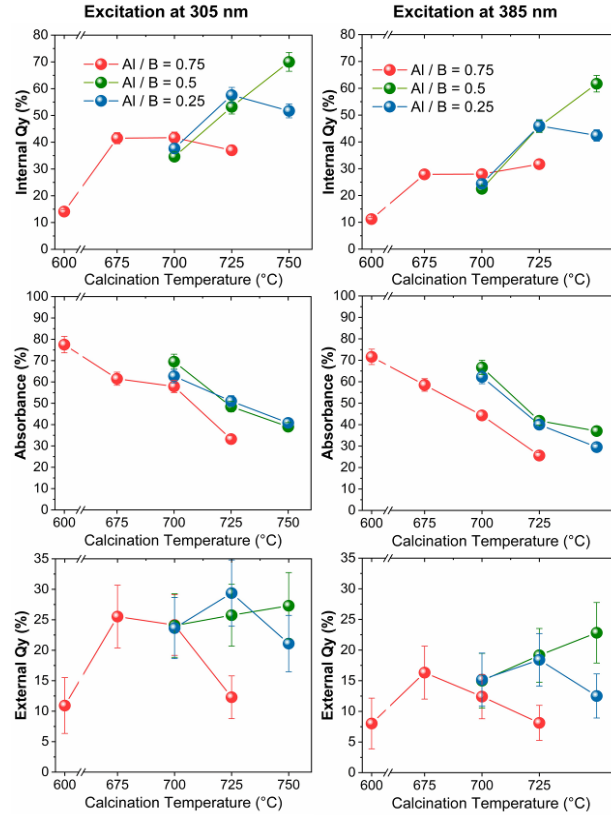


Fig. 5 Internal quantum yield (iQY), optical absorbance (Abs), and external quantum yield (eQY) of the most luminescent ZAB particles with the Al / B ratios of 0.75, 0.5, and 0.25, and T_{Ca} in the range of 600 to 750°C. The phosphors with T_{Ca} leading to poor PL quality due to black carbon are not shown.

iQY increases by raising T_{Ca} and then stabilizes or even decreases slightly. Abs decreases from more than 75% for $T_{Ca} = 600$ °C, to less than 40% for $T_{Ca} = 750$ °C. Consequently, the external quantum yields (eQY) shows a maximum for T_{Ca} ranging from 675 °C to 750°C depending on the Al/B ratio. The increase in iQY by raising T_{Ca} is attributed to the gradual loss of black carbon clusters in the glassy ZAB matrix, as shown in Fig. 1, Fig. S2 and S3. Black carbon is a strong absorber of visible and NUV light. It therefore absorbs, without radiative relaxation, both NUV photons, which would otherwise excite the emitters, and the visible photons from the PL - *i.e.* from the relaxation of excited emitters.

The decrease in the Abs by raising T_{Ca} basically has two main causes. First, similarly to the evolution of iQY, when black carbon is oxidized during the calcination step, it no longer absorbs NUV photons that would otherwise excite the emitters. The lower Abs value recorded for the Al / B = 0.75 is consistent with an earlier release of trapped carbon shown in Fig. S2. Secondly, the origin of the

luminescence is attributed to molecular emitters (see next section), which are very likely also oxidised further by raising T_{Ca} , resulting in the loss of photoluminescence. Finally, the similar PL, iQY and Abs of ZAB phosphors with the Al / B ratios of 0.25 and 0.5 are consistent with their similar structural properties.

To conclude, internal and external QY as well as trichromatic coordinates of elaborated ZAB powders are presented in [Table S1](#) and show that they are suitable for pc-WLED in the single phosphor configuration. Boron-rich phosphors (*i.e.* Al / B = 0.5 - 0.25) are more efficient than Al-rich ones, with both the best compromise between a high eQY and a warm colour temperature obtained for T_{Ca} = 700°C, and the most efficient cold-white emissions for T_{Ca} = 725°C, having a high iQY of 49% when excited at 385 nm. If the iQY values of 50% is nowadays regularly reached in top-tier carbon-based phosphors emitting blueish light,⁵²⁻⁵⁴ it is particularly high for white-emitting phosphors.⁵⁵ While the excitation of ZAB phosphors at 305 nm offers even higher QYs, it however leads to a very bluish emission, as shown in Fig. S15, due to the excitation-dependent emission mechanisms described in the next section. Moreover, technically, the loss in eQY at higher excitation wavelengths in the NUV would be compensated by the higher efficiency of the current LEDs emitting at 385 nm compared to those emitting at 305 nm.

Photoluminescence excitation

A detailed investigation of the PL excitation of ZAB phosphors is presented here, providing new insights into the molecular origin of PL. Indeed, if the emission of polycyclic aromatic hydrocarbon molecules have clearly been observed in YAB phosphor synthesized by sol-gel methods,³² the molecular origin of the PL of YAB phosphors by the PP method has only been suggested from time-resolved PL studies.⁵⁶ The PL spectra of ZAB phosphors with the Al / B ratios of 0.75 and 0.5, recorded for excitations ranging from 250 to 550 nm have been compiled to form excitation-emission maps as shown in Fig. 6. The overall T_{Ca} -dependent behaviour of the PL is in good agreement with Fig. 4, with a shift of the emission band towards shorter wavelengths (*i.e.* blue shift), for all excitation wavelengths. We can also observe the strong effect of the chemical composition on the PL properties, as the increase in the Al / B ratio of ZAB phosphors for a given T_{Ca} of 700 and 725 °C causes a strong

blue shift in PL spectra, for all excitation wavelengths. Consistently, excitation-emission maps of ZAB phosphors with the Al / B ratio of 0.25 (shown in Fig. S16) are very similar to that of 0.5. It should be noted that the ZAB can be efficiently excited in a wide wavelength range compatible with UV and blue commercial LED.

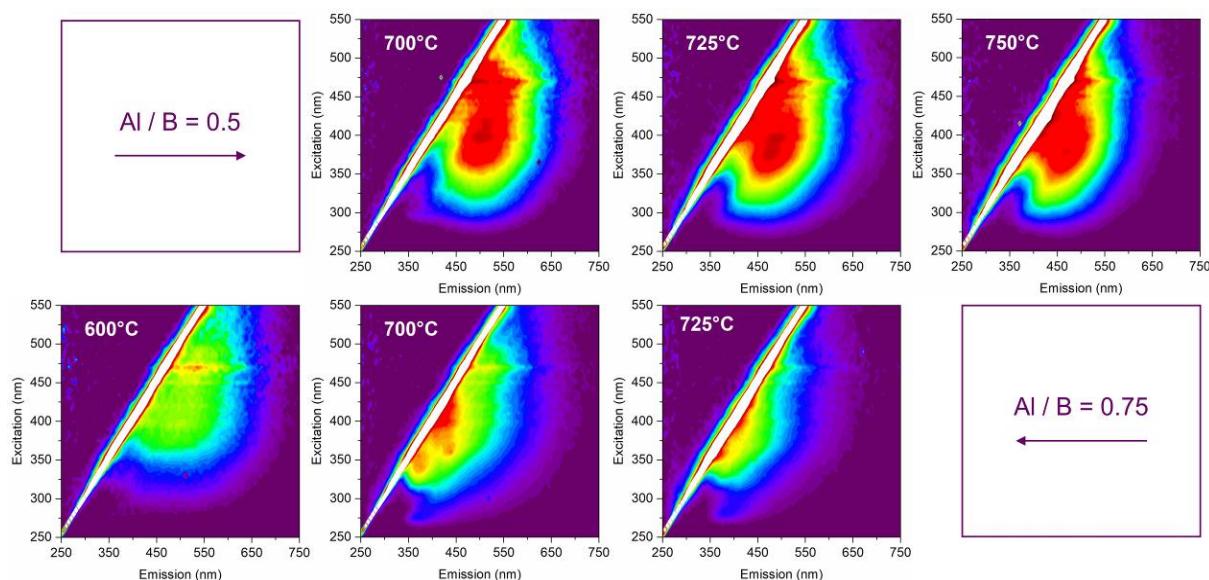


Fig. 6 Excitation-emission maps of ZAB phosphors with the Al / B ratio of 0.5 and 0.75, and calcination temperature in the range of 700 to 750°C and 600 to 725°C, respectively. The emission spectra were recorded for excitation with a step of 5 nm, from 250 to 550 nm. Relative intensities are indicated by a rainbow coloured map, with red being the most intense, and dark purple the least intense, to show the variation in emission for each λ_{exc} . The higher intensities for excitation at 450 and 470 nm are measurement artefacts.

Interestingly, these excitation-emission maps show an excitation-dependent emission for all phosphors, typically observed in small graphene oxide derivatives (GODs) and larger carbon nano-dots (CNDs).⁵⁷ This feature is attributed to the presence of many different GODs / CNDs, having each different radiative energy states. Thus, the set of excited GODs / CNDs varies with the excitation wavelength, and the PL spectra varies accordingly. This diversity of energy states in GODs / CNDs is classically attributed to their size: due to quantum confinement, a small sized GODs / CNDs has a wide energy gap and vice versa.^{55,58,59} Therefore it is often argued that excitation-dependent emission is a signature of a polydispersity of GODs / CNDs size.

If luminescent molecular species are primarily suspected in the case of ZAB phosphors, the analogy with GODs / CNDs is supported by recent results showing the molecular origin of the PL in GODs / CNDs synthesised by chemical methods.^{60–63} Thus, the measured excitation-dependent emission may also indicate a broad distribution of luminescent molecular species, and the blue shift of the PL with increasing T_{Ca} could be attributed to the degradation of luminescent molecular species with a small energy gap (larger entities), favouring the wide energy gap ones (smaller entities). Accordingly, in Fig.6, the emission for excitation in the range of 500-550 nm, ascribed to luminescent molecular species with a small energy gap, vanishes as T_{Ca} is raised. Overall, the blue shift of the emission band of ZAB phosphor is systematically associated with a loss of carbon, which is either due to an increase in T_{Ca} (fig. S3) or to an increase in the Al / B ratio of ZAB particles that traps less carbon (Fig. S2) due to a more open amorphous network. During the calcination, larger carbonaceous species characterized by small energy gaps would be more fragile and sensitive to degradation, especially when the amorphous matrix is less dense. Finally it should be noted that the broad emitting phosphors exhibit a lower excitation-dependent emission effect. We attribute this to the reabsorption of most energetic emissions (350 to 450 nm) by molecular emitter with small energy gaps.

Eventually, calibrated room-temperature PLE spectra of phosphors with the Al / B ratios of 0.5 and 0.75 are shown in Fig. 7, for calcination at 700 and 750 °C, and at 600 and 700 °C, respectively. The excitation profiles were recorded for $\lambda_{em}= 500$ nm, *i.e.* 20000 cm^{-1} . For both compositions, a very broad excitation signal was obtained, deconvoluted into three Gaussian functions centred around 25100 , 28500 , and 31600 cm^{-1} (400, 350 and 316 nm). These excitation profiles further evidence the existence of several emitting centres, located in various local environments⁶⁴ due to the amorphous network. Such multi-excitation states together with an excitation-dependent emission have been observed in carbon dots prepared by hydrothermal synthesis, and also attributed to the presence of several different luminescent molecular species.^{61–63}

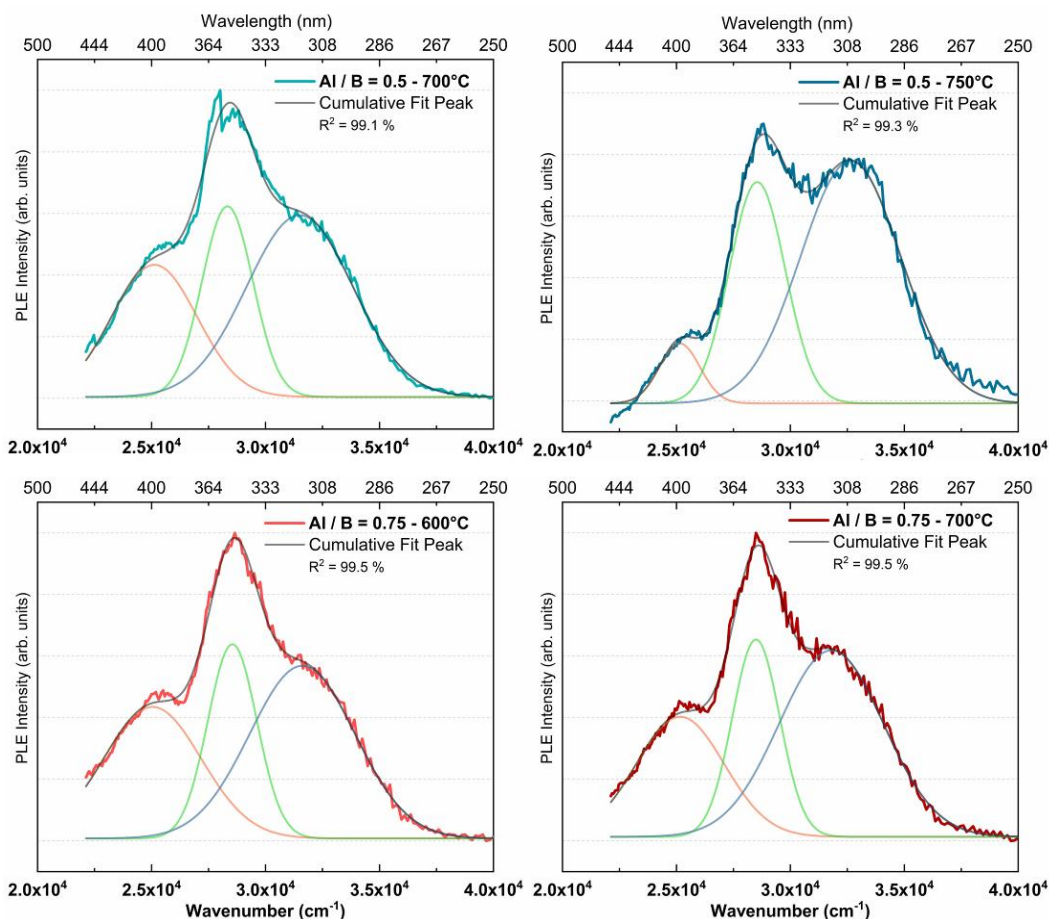


Fig. 7 PLE spectra of ZAB phosphors with Al / B ratio of 0.5 and 0.75, and calcinated at the temperature of 700 and 750 °C, and 600 and 700 °C, respectively. The spectra were fitted with three Gaussian functions as a function of the energy, and corresponding wavelength indicated.

For both compositions, the increase in T_{Ca} results in a decrease in the low-energy excitation at 25100 cm^{-1} (0.63 eV), to the favour of high-energy excitation at 31600 cm^{-1} (1.44 eV), in particular for the phosphors with the Al / B ratio of 0.5 (Table S3). This modification of the excitation supports the hypothesis of the degradation of large luminescent molecular species with small energy gap, to the favour of smaller luminescent molecular species with larger energy gap. Finally, despite a 100 °C difference in T_{Ca} , excitation spectra (Fig. 7) and excitation-emission maps (Fig. 6) of ZAB phosphors with Al / B = 0.5, T_{Ca} = 700°C and Al / B = 0.75, T_{Ca} = 600°C appear similar, suggesting that a boron-rich matrix not only traps carbon more strongly, but also preserves the small energy gap emitting species (*i.e.* large luminescent molecular species) at higher temperature.

It should be noted here that the only attribution of the optical shifts to the size of the luminescent molecular species is a simplification, as their stacking⁶⁵, surface states⁶⁶, and local environment⁶⁴, also affecting their optical transitions, can be modified during the calcination process. The three Gaussian functions fit does not represent only three optically active luminescent molecular species, but rather many, separated into three energy gap ranges.

Alternatively, the high-energy excitation at 31600 cm^{-1} could be attributed to defects in the matrix, that excite luminescent molecular species, responsible for the warmer part of the PL spectra. This combination has been observed by Gan *et al.* in the case of graphene oxide prepared by the Hummers method.⁶⁷

Those results further support the hypothesis of the presence of luminescent molecular species trapped in the micrometric amorphous ZAB and YAB particles, although their clear identification has so far been lacking.

CONCLUSIONS

The PP method has been used to synthesize ZAB phosphors, successfully substituting the yttrium cation by zinc cation in well-described YAB phosphors. The composition has been optimized for a given ZnO molar content of 12%, and by varying the Al / B ratio ranging from 0.25 to 0.75, leading to strongly luminescent powders with broad emission and excitation spectra.

The luminescence appears as the black carbon (strong absorber in the visible) inside the particles is gradually removed during calcination, then shifts from yellowish to bluish by raising the calcination temperature, and eventually disappears gradually between 725 and 800 °C, as the luminescent molecular species are finally decomposed (oxidized) during the matrix crystallization.

The excitation-dependant behaviour of the photoluminescence, as well as the broad excitation band demonstrate a large amount of radiative energy levels, attributed to a wide variety of molecular luminescent species trapped during their formation in the amorphous matrix of ZAB particles upon calcination. The blue shift of the PL by raising the calcination temperature is attributed to the modification of the nature or distribution of such carbon-based luminescent species, resulting in an increase in the mean energy of the optical transitions. Modifying the Al / B ratio during synthesis results in a strong modification of the morphology and microstructure of ZAB particles. In particular, carbonaceous species are more strongly trapped in the ZAB matrix when the boron content is increased due to a denser packing of the amorphous network. This leads to a red shift of the PL, suggesting that large luminescent molecular species with smaller energy gap are preserved.

It should be noted that without optimization of light absorption and extraction, the eQY values are still high, ranging from 15 to 25% depending on the excitation wavelength. Given the low cost of the precursors and the up-scalable synthesis, we believe that further device optimization would result in competitive rare-earth-free phosphors suitable for NUV-LEDs based devices.

These findings report the impact of the microstructure on luminescence of metal borates, which can be applied to engineer other inorganic oxide fabricated by the PP method, provided they can maintain an amorphous structure up to a high enough temperature so the black carbon is removed, while having a dense network to trap luminescent molecular species.

CONFLICTS OF INTEREST

There are no conflicts to declare.

ACKNOWLEDGMENTS

P. G. held a doctoral fellowship from the CDP Eco-SESA CDP Eco-SESA receiving fund from the French National Research Agency in the framework of the "Investissements d'avenir" program (ANR-15-IDEX-02). The authors further acknowledge the facilities, and the scientific and technical assistance of the CMTC characterization platform of Grenoble INP, which is supported by the Centre of Excellence of Multifunctional Architected Materials (LabEx CEMAM) under the contract ANR-10-LABX-44-01 funded by the "Investments for the Future" Program. This research was also funded by Institut Carnot "Energies du Futur" through the "ECOLED" project.

NOTES AND REFERENCES

- 1 S. Nakamura and M. R. Krames, *Proc. IEEE*, 2013, **101**, 2211–2220.
- 2 J. Y. Tsao, M. H. Crawford, M. E. Coltrin, A. J. Fischer, D. D. Koleske, G. S. Subramania, G. T. Wang, J. J. Wierer and R. F. Karlicek, *Adv. Opt. Mater.*, 2014, **2**, 809–836.
- 3 J. Cho, J. H. Park, J. K. Kim and E. F. Schubert, *Laser Photonics Rev.*, 2017, **11**, 1600147.
- 4 N. C. George, A. J. Pell, G. Dantelle, K. Page, A. Llobet, M. Balasubramanian, G. Pintacuda, B. F. Chmelka and R. Seshadri, *Chem. Mater.*, 2013, **25**, 3979–3995.
- 5 X. Qin, X. Liu, W. Huang, M. Bettinelli and X. Liu, *Chem. Rev.*, 2017, **117**, 4488–4527.
- 6 European Commission, *Study on the review of the list of critical raw materials*, 2017.
- 7 U. S. Geological Survey, in *Mineral Commodity Summaries*, 2019, p. 200p.
- 8 D. Chiriu, L. Stagi, C. M. Carbonaro and P. C. Ricci, *Phys. Status Solidi Curr. Top. Solid State Phys.*, 2016, **13**, 989–997.
- 9 C. C. Pavel, A. Marmier, E. Tzimas, T. Schleicher, D. Schüler, M. Buchert and D. Blagoeva, *Phys. Status Solidi Appl. Mater. Sci.*, 2016, **213**, 2937–2946.
- 10 P. F. Smet, A. B. Parmentier and D. Poelman, *J. Electrochem. Soc.*, 2011, **158**, R37.
- 11 M. Shang, C. Li and J. Lin, *Chem. Soc. Rev.*, 2014, **43**, 1372–1386.
- 12 Y. Zhuo, A. Mansouri Tehrani, A. O. Oliynyk, A. C. Duke and J. Brgoch, *Nat. Commun.*, 2018, **9**, 1–10.
- 13 A. A. Bol, R. Van Beek and A. Meijerink, *Chem. Mater.*, 2002, **14**, 1121–1126.
- 14 C. Zhang and J. Lin, *Chem. Soc. Rev.*, 2012, **41**, 7938–7961.
- 15 W. H. Green, K. P. Le, J. Grey, T. T. Au and M. J. Sailor, *Science (80-.)*, 1997, **276**, 1826–1828.
- 16 V. Bekiari and P. Lianos, *Langmuir*, 1998, **14**, 3459–3461.
- 17 C. K. Lin, Y. Luo, H. You, Z. Quan, J. Zhang, J. Fang and J. Lin, *Chem. Mater.*, 2006, **18**, 458–464.
- 18 H. MASAI, *J. Ceram. Soc. Japan*, 2013, **121**, 150–155.
- 19 F. Gu, S. F. Wang, M. K. Lü, G. J. Zhou, D. Xu and D. R. Yuan, *J. Phys. Chem. B*, 2004, **108**, 8119–8123.

- 20 M. Anicete-Santos, F. C. Picon, M. T. Escote, E. R. Leite, P. S. Pizani, J. A. Varela and E. Longo, *Appl. Phys. Lett.*, 2006, **88**, 211911–211914.
- 21 C. Lin, M. Yu, Z. Cheng, C. Zhang, Q. Meng and J. Lin, *Inorg. Chem.*, 2008, **47**, 49–55.
- 22 L. S. Cavalcante, J. C. Sczancoski, J. W. M. Espinosa, V. R. Mastelaro, A. Michalowicz, P. S. Pizani, F. S. De Vicente, M. S. Li, J. A. Varela and E. Longo, *J. Alloys Compd.*, 2009, **471**, 253–258.
- 23 N. Chouhan, C. C. Lin, S. F. Hu and R. S. Liu, *J. Mater. Chem. C*, 2015, **3**, 1473–1479.
- 24 Y. Kaihatsu, W. N. Wang, F. Iskandar and K. Okuyama, *Mater. Lett.*, 2010, **64**, 836–839.
- 25 T. Hasegawa, Y. Abe, A. Koizumi, T. Ueda, K. Toda and M. Sato, *Inorg. Chem.*, 2018, **57**, 857–866.
- 26 X. Zhang, Z. Lu, H. Liu, J. Lin, X. Xu, F. Meng and C. Tang, *J. Mater. Chem. C*, 2015, **3**, 3311–3317.
- 27 W. N. Wang, T. Ogi, Y. Kaihatsu, F. Iskandar and K. Okuyama, *J. Mater. Chem.*, 2011, **21**, 5183–5189.
- 28 T. Ogi, Y. Kaihatsu, F. Iskandar, W. N. Wang and K. Okuyama, *Adv. Mater.*, 2008, **20**, 3235–3238.
- 29 S. N. Baker and G. A. Baker, *Angew. Chemie - Int. Ed.*, 2010, **49**, 6726–6744.
- 30 V. F. Guimarães, L. J. Q. Maia, I. Gautier-Luneau, C. Bouchard, A. C. Hernandez, F. Thomas, A. Ferrier, B. Viana and A. Ibanez, *J. Mater. Chem. C*, 2015, **3**, 5795–5802.
- 31 V. F. Guimarães, A. D. Sontakke, L. J. Q. Maia, M. Salaün, I. Gautier-Luneau, A. Ferrier, B. Viana and A. Ibanez, *J. Lumin.*, 2017, **188**, 448–453.
- 32 P. Burner, A. D. Sontakke, M. Salaün, M. Bardet, J. M. Mouesca, S. Gambarelli, A. L. Barra, A. Ferrier, B. Viana, A. Ibanez, V. Maurel and I. Gautier-Luneau, *Angew. Chemie - Int. Ed.*, 2017, **56**, 13995–13998.
- 33 P. P. Neves, L. J. Q. Maia, M. I. B. Bernardi, A. R. Zanatta, V. R. Mastelaro, S. M. Zanetti and E. R. Leite, *J. Sol-Gel Sci. Technol.*, 2004, **29**, 89–96.
- 34 K. Nose and M. Zenki, *Analyst*, 1991, **116**, 711–714.
- 35 V. F. Guimarães, M. Salaün, P. Burner, L. J. Q. Maia, A. Ferrier, B. Viana, I. Gautier-Luneau and A. Ibanez, *Solid State Sci.*, 2017, **65**, 6–14.
- 36 J. Lin, M. Yu, C. Lin and X. Liu, *J. Phys. Chem. C*, 2007, **111**, 5835–5845.
- 37 G. E. Brown, F. Farges and G. Calas, *Rev. miner.*, 1995, **32**, 317–410.
- 38 A. Nukui, U. Shimizugawa, S. Inoue, H. Ozawa, R. Uno, K. Oosumi and A. Makishima, *J. Non. Cryst. Solids*, 1992, **150**, 376–379.
- 39 A. Dietzel, *Glasstruktur und Glaseigenschaften*, Glastechn. Ber. 22, 1948.
- 40 T. Jawhari, A. Roid and J. Casado, *Carbon N. Y.*, 1995, **33**, 1561–1565.
- 41 A. Merlen, J. G. Buijnsters and C. Pardanaud, *A guide to and review of the use of multiwavelength Raman spectroscopy for characterizing defective aromatic carbon solids: From graphene to amorphous carbons*, 2017, vol. 7.
- 42 A. Ferrari and J. Robertson, *Phys. Rev. B - Condens. Matter Mater. Phys.*, 2000, **61**, 14095–14107.
- 43 V. F. Guimarães, P. Burner, L. J. Q. Maia, A. Ferrier, B. Viana, I. Gautier-Luneau and A. Ibanez, *Proc. SPIE*, 2016, **9749**, 97490B.
- 44 E. M. Elssfah, C. C. Tang, J. Zhang, H. S. Song, X. X. Ding and S. R. Qi, *Mater. Res. Bull.*, 2007, **42**, 482–486.
- 45 T. Ogi, H. Iwasaki, A. B. D. Nandiyanto, F. Iskandar, W. N. Wang and K. Okuyama, *J. Mater. Chem. C*, 2014, **2**, 4297–4303.

- 46 K. Januchta, R. E. Youngman, A. Goel, M. Bauchy, S. J. Rzoska, M. Bockowski and M. M. Smedskjaer, *J. Non. Cryst. Solids*, 2017, **460**, 54–65.
- 47 N. Mascaraque, K. Januchta, K. F. Frederiksen, R. E. Youngman, M. Bauchy and M. M. Smedskjaer, *J. Am. Ceram. Soc.*, 2019, **102**, 1157–1168.
- 48 A. A. Osipov, V. E. Eremyashev, A. S. Mazur, P. M. Tolstoi and L. M. Osipova, *Glas. Phys. Chem.*, 2016, **42**, 230–237.
- 49 C. Zhu, X. Nai, D. Zhu, F. Guo, Y. Zhang and W. Li, *J. Solid State Chem.*, 2013, **197**, 1–6.
- 50 Å. Johan, S. Göran and G. Jekabs, *Acta Chem. Scand.*, 1997, **51**, 1045–1050.
- 51 K. L. Wong, J. C. G. Bünzli and P. A. Tanner, *J. Lumin.*, 2020, **224**, 117256.
- 52 F. Ehrat, S. Bhattacharyya, J. Schneider, A. Löf, R. Wyrwich, A. L. Rogach, J. K. Stolarczyk, A. S. Urban and J. Feldmann, *Nano Lett.*, 2017, **17**, 7710–7716.
- 53 D. Wang, Z. Wang, Q. Zhan, Y. Pu, J. X. Wang, N. R. Foster and L. Dai, *Engineering*, 2017, **3**, 402–408.
- 54 D. Qu, M. Zheng, L. Zhang, H. Zhao, Z. Xie, X. Jing, R. E. Haddad, H. Fan and Z. Sun, *Sci. Rep.*, 2014, **4**, 1–11.
- 55 X. Guo, C. F. Wang, Z. Y. Yu, L. Chen and S. Chen, *Chem. Commun.*, 2012, **48**, 2692–2694.
- 56 A. D. Sontakke, A. Ferrier, P. Burner, V. F. Guimarães, M. Salaün, V. Maurel, I. Gautier-Luneau, A. Ibanez and B. Viana, *J. Phys. Chem. Lett.*, 2017, **8**, 4735–4739.
- 57 Z. Gan, H. Xu and Y. Hao, *Nanoscale*, 2016, **8**, 7794–7807.
- 58 H. Li, X. He, Z. Kang, H. Huang, Y. Liu, J. Liu, S. Lian, C. H. A. Tsang, X. Yang and S. T. Lee, *Angew. Chemie - Int. Ed.*, 2010, **49**, 4430–4434.
- 59 C. Russo, B. Apicella and A. Ciajolo, *Sci. Rep.*, 2019, **9**, 14566.
- 60 L. Shi, J. H. Yang, H. B. Zeng, Y. M. Chen, S. C. Yang, C. Wu, H. Zeng, O. Yoshihito and Q. Zhang, *Nanoscale*, 2016, **8**, 14374–14378.
- 61 M. Fu, F. Ehrat, Y. Wang, K. Z. Milowska, C. Reckmeier, A. L. Rogach, J. K. Stolarczyk, A. S. Urban and J. Feldmann, *Nano Lett.*, 2015, **15**, 6030–6035.
- 62 S. Bhattacharyya, F. Ehrat, P. Urban, R. Teves, R. Wyrwich, M. Döblinger, J. Feldmann, A. S. Urban and J. K. Stolarczyk, *Nat. Commun.*, 2017, **8**, 1–9.
- 63 C. M. Carbonaro, D. Chiriu, L. Stagi, M. F. Casula, S. V Thakkar, L. Malfatti, K. Suzuki, P. C. Ricci and R. Corpino, *J. Phys. Chem. C*, 2018, **122**, 25638–25650.
- 64 S. Park, E. K. Ji, H. K. Se, J. Seo, K. Chung, S. Y. Park, D. J. Jang, B. M. Medina, J. Gierschner and Y. P. Soo, *J. Am. Chem. Soc.*, 2009, **131**, 14043–14049.
- 65 M. Baroncini, G. Bergamini and P. Ceroni, *Chem. Commun.*, 2017, **53**, 2081–2093.
- 66 H. Ding, S. B. Yu, J. S. Wei and H. M. Xiong, *ACS Nano*, 2016, **10**, 484–491.
- 67 Z. Gan, S. Xiong, X. Wu, T. Xu, X. Zhu, X. Gan, J. Guo, J. Shen, L. Sun and P. K. Chu, *Adv. Opt. Mater.*, 2013, **1**, 926–932.